

Complex Dyadic Multiresolution Analyses

J.-M. Lina, P. Turcotte and B. Goulard

Network for Computing and Mathematical Modelling

Centre de Recherches Mathématiques, Univ. de Montréal

C.P. 6128 Succ. Centre-Ville, Montréal, Québec H3C 3J7, Canada

CRM-2564 (August 1998)

Abstract

This paper presents the construction and some properties of the symmetric daubechies wavelets. This class of solutions is part of the set of complex-valued solutions of the daubechies' program: orthonormal bases of L^2 built from compactly supported wavelets with maximum regularity. We review some algorithms that take explicit advantage of the presence of phase in the complex representation of signals by the Symmetric Daubechies Wavelets. Applications for two dimensional signals are discussed.

1 Introduction

Complex-valued fields are very common in physics. Not only because of the extensive use of Fourier representation of physical quantities that helps to solve problems such as the propagation of waves but also because phase can contain non-trivial informations related to interactions and symmetries. Quantum mechanics, non-linear optics, solid state physics illustrate nicely the “role of the phase” in the modelling of physical processes. More recently the Berry-Hannay phase exhibited non-trivial behaviour in the cyclic evolution of quantal or semi-classical systems. However, in comparison, signal processing makes little use of the phase: because the “role of the phase” is less prominent in the Fourier representation of real signals, most of the attention is focused on the amplitude information. Nevertheless, many papers have stressed the “importance of the role of the phase” in various problems in signal processing; furthermore phase are indeed present in many technologies and sometimes play a fundamental role as in holography or quantum cryptography. The objective of this work is to discuss the “role of the phase” in the area of discrete wavelet representations of signals. It is worth noticing that the notion of phase was involved in the early development of the continuous wavelet framework, especially for tracking the local frequency of signals (the so-called *ridge and skeleton algorithm*). Here we consider the complex extension of the famous Daubechies solutions. As mentioned in [19] (used here as the main reference on wavelets), some of these complex solutions exhibit symmetries. This property first motivated our study of complex Daubechies wavelet but from a practical point of view the question remains: why should complex Daubechies wavelets be of interest?

To motivate our presentation, the next two sections discuss the role of the phase in the context of spline wavelet bases. It gives the opportunity to recall basic definitions of a multiresolution analysis used in this paper. Sections 4 and 5 present the Daubechies solutions and the symmetric Daubechies wavelets respectively. Section 6 describes some properties of those solutions that are directly related to the phase of the wavelet. The algorithmic point of view of the complex dyadic wavelet analysis is presented in Section 7. The remaining sections describe some applications of the complex wavelet representation, mainly dedicated to image processing. Finally, a conclusion presents future avenues of research in the field of complex data modeling.

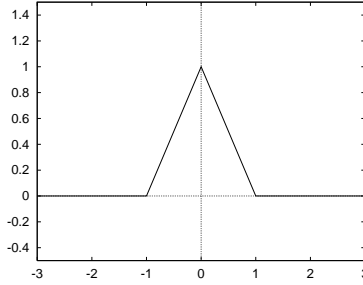


Figure 1: The linear spline function

2 The Spline Example

The “role of the phase” can be nicely illustrated with the well-known wavelet bases associated with the *Linear-Spline function* (Fig.1). We take the opportunity of this introductory example for presenting some basic definitions used all along this work. More details can be found in [8] and [19].

We start with the definition of an **approximation space**, say V_0 , endowed with a **Riesz basis** $\{\varphi_k, k \in \mathbb{Z}\}$:

$$f(x) \in V_0, \quad f(x) = \sum_k c_k \varphi_k(x) \quad (1)$$

where $\varphi_k(x) = \varphi(x - k)$. φ is the **scaling function** normalized with unit integral. The set of functions φ_k is linearly independent and provides a complete and stable representation of V_0 : $A > 0$ and finite B exist such that

$$A\|f\|_2^2 \leq \sum_k |\langle f | \varphi_k \rangle|^2 \leq B\|f\|_2^2 \quad (2)$$

This property (Riesz) will be more characterized in a sequel. A simple example of such a basis is given by the *Linear-Spline function* (Fig.1),

$$s(x) = \sup(1 - |x|, 0). \quad (3)$$

The integer translates of $s(x)$ span an approximation space:

$$f(x) = \sum_k c_k s(x - k) \quad (4)$$

where here $c_k = f(k)$ since splines are interpolatory functions. In other words, any continuous function f can be linearly approximated through an expansion in this approximation space V_0 . The property (2) can be characterized in the Fourier domain. Defining

$$\sigma_\varphi(\omega) = \sum_p |\hat{\varphi}(\omega + 2\pi p)|^2 \quad (5)$$

where $\hat{\varphi}$ is the Fourier transform of the scaling function, Eq.(2) amounts the inequalities $0 < \sigma_\varphi(\omega) < \infty$ (see [19], p.222). For instance, we have

$$\frac{1}{3} \leq \sigma_s(\omega) = \frac{2 + \cos \omega}{3} \leq 1 \quad (6)$$

for the linear spline (3) whose Fourier representation is

$$\hat{s}(\omega) = \left(\frac{\sin(\frac{\omega}{2})}{\frac{\omega}{2}} \right)^2 \quad (7)$$

Looking for an orthonormal basis for V_0 , the *orthonormalisation* of the Riesz basis is easily done in the Fourier domain since it is equivalent to find a basis constructed from a scaling function for which $\sigma_\varphi(\omega) = 1$ (see [19], p.225). Such a condition is not fulfilled with the spline (4), however, writing

$$\sigma_s(\omega) = u(\omega)\overline{u(\omega)} \quad (8)$$

the new scaling function defined by

$$\hat{\varphi}(\omega) = \frac{\hat{s}(\omega)}{u(\omega)} \quad (9)$$

obviously satisfies $\sigma_\varphi(\omega) = 1$ and defines an orthonormal basis of V_0 . Various **factorizations** of $\sigma_s(\omega)$ define different scaling functions φ through the phase of $u(\omega)$. In the spline example discussed here, a first factorization has been proposed by Stromberg [22]:

$$\sigma_s(\omega) = |u_1(\omega)|^2 \quad \text{with} \quad u_1(\omega) = \frac{3 + \sqrt{3}}{6}(1 + re^{i\omega}), \quad r = 2 - \sqrt{3} \quad (10)$$

The associated scaling function is displayed in Fig.2. Later, Battle in [3] and Lemarié in [18] have considered an other factorization

$$\sigma_s(\omega) = |u_2(\omega)|^2 \quad \text{with} \quad u_2(\omega) = \sqrt{\frac{2 + \cos \omega}{3}} = u_1(\omega) e^{i\xi(\omega)} \quad (11)$$

The phase $\xi(\omega)$ introduces an extra property into the new scaling function: $\varphi(x) = \varphi(-x)$, i.e. **symmetry**, as illustrated in Fig.2. Both factorizations yield orthonormal sets $\{\varphi_k\}$ but the solution of Battle and Lemarié leads to a symmetric scaling function. We notice that orthonormalization of the spline basis has ruined off the original compactness of the support of the spline scaling function. In the next section, it will be shown that compactness of the support (i.e. strong locality in space), orthogonality of the basis and symmetry are all met in the seminal Daubechies framework *if* we relax the implicit condition on the reality of the scaling functions. Indeed, all found solutions are complex-valued.

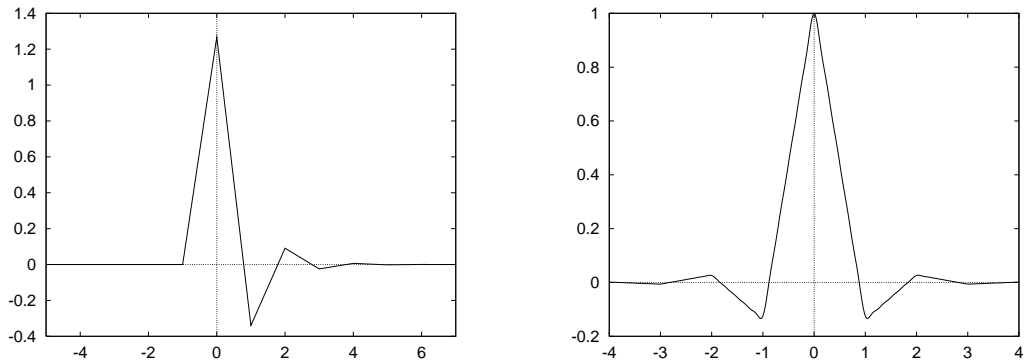


Figure 2: The Stromberg scaling function (left) and the Battle-Lemarié scaling function (right) for the linear spline.

3 Multiresolution and Wavelet

A dyadic multiresolution is based on a **scaling function** φ that obeys a **refinement equation**

$$\varphi(x) = 2 \sum_k a_k \varphi(2x - k) \quad (12)$$

where the a_k 's are complex-valued coefficients such that $\sum a_k = 1$. This functional equation relates the spanning function at *different* scales. For

instance, the spline defined by Eq.(3) does satisfy such a relation:

$$s(x) = \frac{1}{2}s(2x - 1) + s(x) + \frac{1}{2}s(2x + 1) \quad (13)$$

It is worth rewriting Eq.(12) in the Fourier domain and defining the trigonometric polynomial

$$m_0(\omega) = \sum_k a_k e^{ik\omega}, \quad (14)$$

usually called **filter** associated with the scaling function. Eq.(12) can be written as

$$\hat{\varphi}(\omega) = m_0\left(\frac{\omega}{2}\right)\hat{\varphi}\left(\frac{\omega}{2}\right) \quad (15)$$

Most of the properties of the scaling function can be computed from $m_0(\omega)$ (see [19]). For example, the filter associated with the spline (3) is

$$m_0(\omega) = \left(\cos \frac{\omega}{2}\right)^2 = \left(\frac{1 + e^{i\omega}}{2}\right)^2 e^{-i\omega} \quad (16)$$

and the solutions of Stromberg (10) and Battle-Lemarié (11) are associated with the filters

$$m_0(\omega) \frac{u_1(\omega)}{u_1(2\omega)} \quad \text{and} \quad m_0(\omega) \frac{u_1(\omega)}{u_1(2\omega)} e^{-i(\xi(\omega) - \xi(2\omega))} \quad (17)$$

respectively. The extra factors at the right of $m_0(\omega)$ insure the orthogonality property $\sigma_\varphi(\omega) = 1$ of the new bases. We notice that the two filters in Eq.(17) differ only by a phase: this is the origin of the symmetry exhibited by the Battle-Lemarié solution. Indeed, the orthogonality condition can be recast in terms of the amplitude of $m_0(\omega)$:

$$|m_0(\omega)|^2 + |m_0(\omega + \pi)|^2 = 1 \quad (18)$$

Thus, it is clear that combining a property like symmetry with orthonormality is a matter of defining a specific phase of the filter.

The scaling relationship expressed by Eq.(12) is related with the definition of the multiresolution analysis of $L^2(\mathbb{R})$ based on φ proposed by Mallat and Meyer. A multiresolution amounts to consider a sequence of closed subspaces $V_j \subset L^2(\mathbb{R})$,

$$V_j \subset V_{j+1}, \quad \bigcap_j V_j = \{0\}, \quad \overline{\bigcup_j V_j} = L^2(\mathbb{R}), \quad (19)$$

such that

$$f(x) \in V_j \Leftrightarrow f(2x) \in V_{j+1} \quad (20)$$

The scaling equation (12) expresses the nested structure of the V_i 's. At any scale $a_j = 2^{-j}$, elements of V_j are of the form

$$\sum_k c_{j,k} \varphi_j(x - ka_j) \quad (21)$$

where $\varphi_j(x)$ is the scaled function $\varphi_j(x) = \frac{1}{\sqrt{a_j}} \varphi\left(\frac{x}{a_j}\right)$. Consequently, the set of functions

$$\varphi_{j,k}(x) = 2^{\frac{j}{2}} \varphi(2^j x - k) \quad (22)$$

constitutes a basis of the approximation space “at scale $a_j = 2^{-j}$ ” when k runs over the integer. Let us remark that if V_0 is endowed with an orthonormal basis, then $\{\varphi_{j,k}, k \in \mathbb{Z}\}$ is also an orthonormal basis for the approximation space V_j . The last step towards wavelets is the following theorem (see [19], p.236): a **wavelet** $\psi \in V_1$ with vanishing integral exists such that $\{\varphi(x - k), \psi(x - k), k \in \mathbb{Z}\}$ is an **orthonormal basis** of V_1 .

Wavelet multiresolution therefore aims to decompose $V_1 = V_0 \oplus W_0$ where W_0 is generated through the integer translates of a function ψ . Since $\psi \in W_0 \subset V_1$, a sequence of complex-valued coefficients b_k exists such that:

$$\psi(x) = 2 \sum_k b_k \varphi(2x - k) \quad (23)$$

or, defining $m_1(\omega) = \sum_k b_k e^{ik\omega}$,

$$\hat{\psi}(\omega) = m_1\left(\frac{\omega}{2}\right) \hat{\varphi}\left(\frac{\omega}{2}\right) \quad (24)$$

It can be shown, using $m_1(\omega) = e^{-3i\omega} \overline{m_0(\omega + \pi)}$, that the set $\{\psi(x - k), k \in \mathbb{Z}\}$ is an orthonormal basis of W_0 . This result amounts taking $b_k = (-1)^k \overline{a_{1-k}}$ in Eq.(23). The orthonormal decomposition of each dyadic approximation space, i.e $V_{j+1} = V_j \oplus W_j$, defines the **details spaces** W_j generated by the set of orthonormal wavelets

$$\{\psi_{j,k}(x) = 2^{\frac{j}{2}} \psi(2^j x - k)\} \quad (25)$$

when k runs over \mathbb{Z} . Altogether, those functions generated by the translates of all dyadic scaling transforms of ψ produce an orthonormal basis of $L^2(\mathbb{R})$:

$$f(x) = \sum_{j=-\infty}^{\infty} \sum_k d_{jk} \psi_{j,k}(x) \quad (26)$$

• **Example: The Spline Wavelets.** The construction of the wavelet associated with the two scaling functions displayed in Fig.1 is straightforward: using the previous expression for $m_1(\omega)$, we obtain

$$\hat{\psi}(\omega) = \overline{u\left(\frac{\omega}{2} + \pi\right)} e^{-\frac{3}{2}i\omega} \frac{\sin\left(\frac{\omega}{4}\right)^4}{\sigma_s\left(\frac{\omega}{2}\right)\left(\frac{\omega}{4}\right)^2} \quad (27)$$

As illustrated in Fig.2, the factorization $\sigma_s w(\omega) = |u_2(\omega)|^2$ gives a symmetric wavelet: $\psi(x) = \psi(1-x)$.

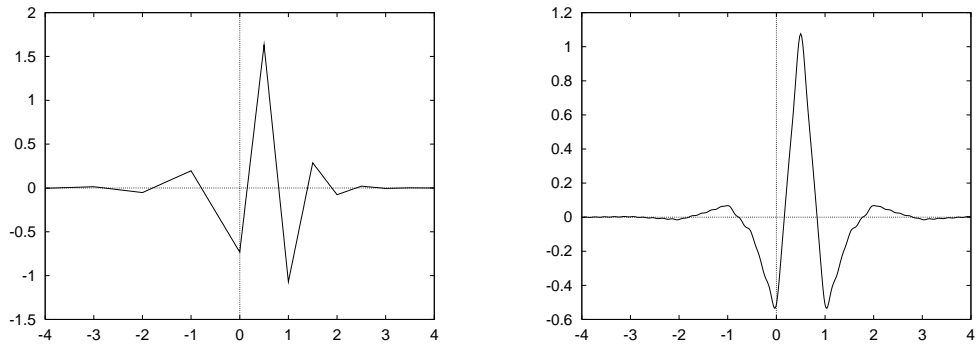


Figure 3: The Stromberg (left) and Battle-Lemarié (right) wavelets.

Those two examples are illustrating nicely the scope of the forthcoming sections: provided we can select an appropriate phase in $\hat{\psi}$, *i.e* in $m_0(\omega)$, a **symmetric scaling function** can be constructed on the multiresolution spaces. The same phase analysis will be carried out in the context of Daubechies wavelets.

Let us make a final comment about the regularity of the multiresolution bases. Let us recall that for orthonormal bases of the form (3), it is *impossible* that ψ has exponential decay in both space and frequency. It will be more

convenient to control the regularity through the polynomial content of the approximation spaces V_j or, equivalently, the **vanishing moments** of the corresponding wavelet (see [19], p.154):

$$\int x^l \psi(x) dx = 0, \quad \text{for } l = 0, 1, \dots, J \quad (28)$$

where J is some integer or, in an equivalent way, the vanishing of the successive derivatives of $\hat{\psi}$ at $\omega = 0$. Using Eq.(24) and the definition of $m_1(\omega)$, the criteria of regularity can be written as

$$\frac{d^l}{d\omega^l} m_0(\omega)|_{\omega=\pi} = 0, \quad \text{for } l = 0, 1, \dots, J \quad (29)$$

This is the Strang-Fix condition (see [19], p.242). As seen in Eq.(16) and Eq.(17), the previous examples illustrate this condition with $J = 2$.

4 Daubechies' Wavelets

Daubechies scaling functions are subject to the following constraints:

- 1) Compactness of the support of φ : We require that φ (and consequently ψ) has a compact support inside the interval $[-J, J + 1]$ for some integer J . This requirement amounts to consider a finite number of terms in the expansion (7): $a_k \neq 0$ for $k = -J, -J + 1, \dots, J, J + 1$.
- 2) Orthogonality of the $\varphi(x - k)$: Instead of working with $m_0(\omega)$ and solving Eq.(18), we define the polynomial

$$F(z) = \sum_{n=-J}^{J+1} a_n z^n, \quad \text{with } F(1) = 1 \quad (30)$$

where z is on the unit circle, $|z| = 1$. The orthonormality condition (18) can be stated through the following equation

$$P(z) - P(-z) = z \quad (31)$$

where the polynomial $P(z)$ is defined as

$$P(z) = zF(z)\overline{F(z)} \quad (32)$$

- 3) Strang-Fix condition: To maximize the regularity of the functions generated by the scaling function φ , we require the vanishing of the first J

moments of the wavelet. In terms of the polynomial (30), the Strang-Fix condition reads as

$$F(-1) = F'(-1) = F''(-1) = \dots = F^{(J)}(-1) = 0 \quad (33)$$

This last condition is satisfied with the polynomial defined by

$$P_J(z) = h(z)^{2J+2} p_J(z^{-1}) \quad (34)$$

where

$$h(z) = \frac{1+z}{2} \quad (35)$$

A solution of the full constraints defined by Daubechies is

$$p_J(z) = \sum_{j=0}^{2J} r_j h(z)^{2J-j} h(-z)^j, \quad \text{with} \quad \begin{cases} r_{2j} = (-1)^j \binom{2J+1}{j}, \\ r_{2j+1} = 0 \end{cases}, \quad j = 0, \dots, J \quad (36)$$

Let us sketch the proof that $P_J(z)$ does satisfy Eq.(31): we first rewrite $P_J(z)$ on the form

$$P_J(z) = \frac{1}{z^{2J}} \sum_{j=0}^J (-1)^j \binom{2J+1}{j} H(-z)^j H(z)^{2J+1-j} \quad (37)$$

where $H(z) = \frac{(1+z)^2}{4}$. Using the equality $\binom{2J+1}{j} = \binom{2J+1}{2J+1-j}$, we obtain

$$P_J(-z) = \frac{1}{z^{2J}} \sum_{j=J+1}^{2J+1} (-1)^{1-j} \binom{2J+1}{j} H(-z)^j H(z)^{2J+1-j} \quad (38)$$

and finally Eq.(31) results trivially by taking the difference of the two last expressions:

$$\begin{aligned} P_J(z) - P_J(-z) &= \frac{1}{z^{2J}} \sum_{j=0}^{2J+1} (-1)^j \binom{2J+1}{j} (-H(-z))^j H(z)^{2J+1-j} \\ &= \frac{1}{z^{2J}} (H(z) - H(-z))^{2J+1} \\ &= z \end{aligned} \quad (39)$$

The relevance of the polynomial $P_J(z)$ in the construction of multiresolution

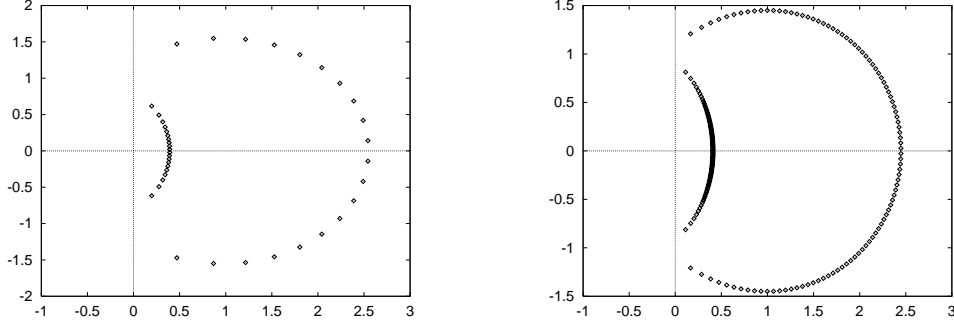


Figure 4: The roots of $p_{12}(z)$ (left) and $p_{100}(z)$ (right).

bases relies on the particular relationship between the $2J$ roots of $p_J(z)$. Indeed, we can write the following factorization of $p_J(z)$:

$$p_J(z) = \prod_{k=1}^J \left(\frac{z - x_k}{1 - x_k} \right) \prod_{k=1}^J \left(\frac{z - \bar{x}_k^{-1}}{1 - \bar{x}_k^{-1}} \right) \quad (40)$$

where $x_{k=1,2,\dots,J}$ are the J roots inside the unit circle, $|x_k| < 1$, and $\Re(x_k) > \Re(x_{k+1})$ (see Fig.3). Writing $F(z)$ as

$$F(z) = \left(\frac{1+z}{2} \right)^{1+J} p(z^{-1}) \quad (41)$$

the polynomial $p(z)$ is defined through some particular roots of $p_J(z)$ and it is easily found that for *any* subset $R \subset \{1, 2, 3, \dots, J\}$ all solutions of the form

$$p(z) = \prod_{m \in R} \left(\frac{z - x_m}{1 - x_m} \right) \prod_{n \notin R} \left(\frac{z - \bar{x}_n^{-1}}{1 - \bar{x}_n^{-1}} \right) \quad (42)$$

factorize $P_J(z) = zF(z)\overline{F}(z)$. Therefore, for any integer J , the trigonometric polynomial given by

$$m_0(\omega) = \left(\frac{1 + e^{i\omega}}{2} \right)^{1+J} \prod_{k \in R} \left(\frac{e^{-i\omega} - x_k}{1 - x_k} \right) \prod_{k \notin R} \left(\frac{e^{-i\omega} - \bar{x}_k^{-1}}{1 - \bar{x}_k^{-1}} \right) \quad (43)$$

with any selection R of roots of $p_J(z)$, defines an admissible trigonometric polynomial and thus a compactly supported orthonormal dyadic wavelet

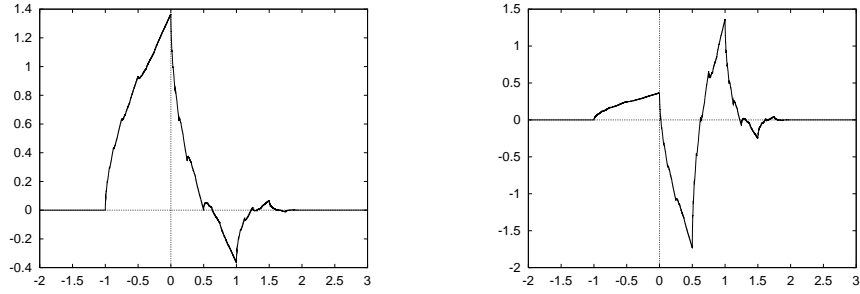


Figure 5: Left: The scaling function φ for $J=1$. Right: The Daubechies wavelet ψ for $J=1$.

basis (with all the material described in Section 3). Let us notice that permuting R and \bar{R} in Eq.(43) is equivalent to replacing a_k by its complex conjugate (up to some trivial translation). So, excepted for the Haar case ($J = 0$, $a_0 = 0.5$ and $a_1 = 0.5$), we obtain 2^{J-1} solutions. In her seminal work [8], Daubechies investigated a subset of this family: she selected R so that the coefficients in the trigonometric expansion $m_0 = \sum_k a_k e^{ik\omega}$ are **real** valued. The usual Daubechies wavelets are thus real valued functions.

- Example $J = 1$: The polynomial $p_1(z)$ has two roots $x_1 = r = 2 - \sqrt{3}$ and x_1^{-1} . The unique solution is thus

$$m_0(\omega) = \left(\frac{1 + e^{i\omega}}{2} \right)^2 \left(\frac{e^{-i\omega} - r}{1 - r} \right) \quad (44)$$

and corresponds to the well-known *DAUB4* wavelet (see Fig.5). Let us note that taking Eq.(44) with $r = 0$ leads precisely to the filter associated with the linear spline, see Eq.(16).

- Example $J = 2$: The polynomial $p_2(z)$ has four roots

$$x_1 = \frac{3}{2} - i\sqrt{\frac{5}{12}} - \frac{1}{2}\sqrt{\frac{10}{3} - 2i\sqrt{15}} \quad (45)$$

$$x_2 = \frac{3}{2} - i\sqrt{\frac{5}{12}} + \frac{1}{2}\sqrt{\frac{10}{3} - 2i\sqrt{15}} \quad (46)$$

and $\bar{x}_1^{-1}, \bar{x}_2^{-1}$. Two distinct cases are found: $R = \{1, 2\}$ and $R = \{1\}$.

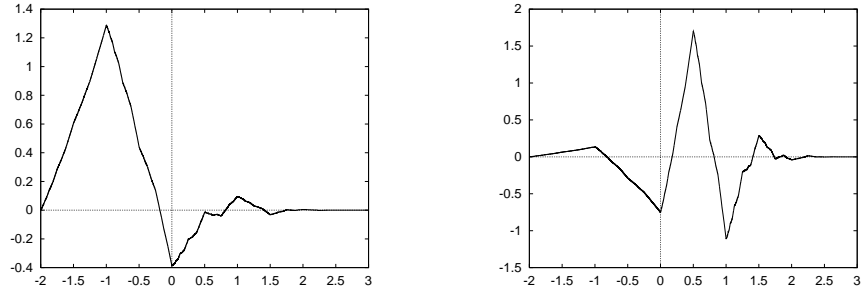


Figure 6: The real scaling function and wavelet (*DAUB6*) for $J=2$.

The first case

$$m_0(\omega) = \left(\frac{1 + e^{i\omega}}{2}\right)^3 \left(\frac{e^{-i\omega} - x_1}{1 - x_1}\right) \left(\frac{e^{-i\omega} - x_2}{1 - x_2}\right) \quad (47)$$

corresponds to the *DAUB6* solution displayed in Fig.6. The second selection of roots gives

$$m_0(\omega) = \left(\frac{1 + e^{i\omega}}{2}\right)^3 \left(\frac{e^{-i\omega} - x_1}{1 - x_1}\right) \left(\frac{e^{-i\omega} - \bar{x}_2^{-1}}{1 - \bar{x}_2^{-1}}\right) \quad (48)$$

As anticipated by Lawton (see [8], p.253 and [13]), this solution leads to **symmetric** but **complex-valued** scaling function and wavelet (see Fig.7).

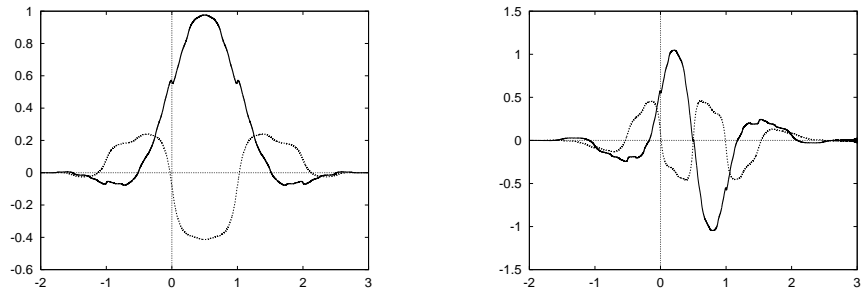


Figure 7: The complex scaling function (left) and wavelet (right) for $J=2$ (Imaginary part indicated by a dashed line).

Such complex solutions exist for any value of J but symmetry is only possible with J **even**. In the next section we will consider a particular family of Daubechies symmetric solutions. Let us however mention the existence of the solution displayed in Fig.8 for which $J = 6$. Two things must be noted: the functions have a small imaginary part and a real part that bears a close resemblance to the Battle-Lemarié orthogonal basis associated with the quadratic spline (see [8], p.150). Let us mention that, despite its complex value, the solution displayed on Fig.8 has demonstrated nice performance in image compression (see [4]).

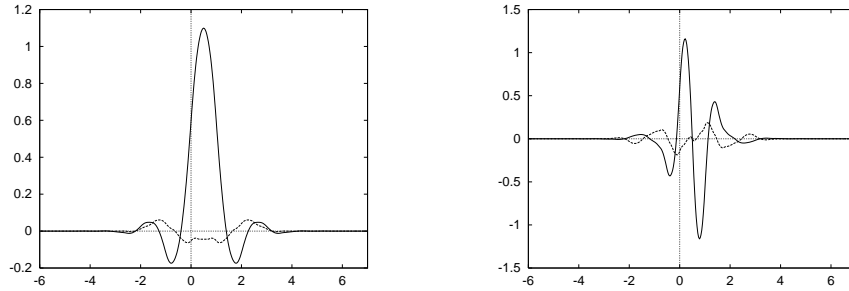


Figure 8: A complex scaling function (left) and wavelet (right) for $J=6$ (Imaginary part indicated by a dashed line).

5 Symmetric Daubechies Wavelets

The symmetry $\varphi(x) = \varphi(1 - x)$ defines a subset of solutions corresponding to the following rule of selection for the roots in Eq.(43):

$$k \in R \iff J - k + 1 \notin R \quad (49)$$

We first notice that symmetry rules out the “reality” of the scaling function: all the symmetric Daubechies wavelets are complex-valued and for any even value of J , $2^{\frac{J-1}{2}}$ distinct solutions exist. In the present work, we consider a particular family of solutions, the so-called *SDWJ* Daubechies wavelets, that correspond to the following selection of roots:

$$R = \{1, 3, 5, \dots, 2k + 1, \dots, J - 1\} \quad (50)$$

that clearly satisfies the rule (49). For $J = 2$, the solution (SDW2) is shown on Fig.7. Fig.9 and Fig.10 display the two complex solutions for $J = 4$ (SDW4 corresponds to Fig.10).

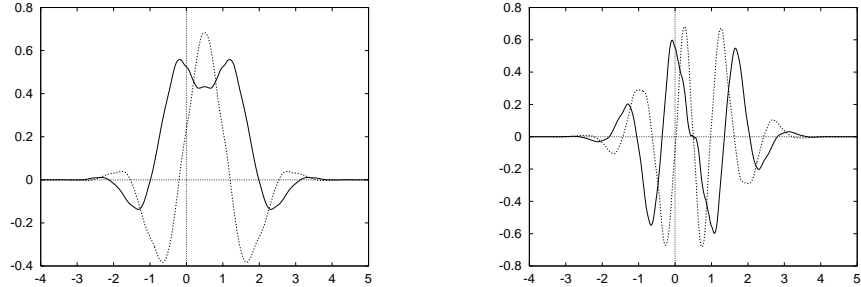


Figure 9: Complex scaling function (left) and wavelet (right) for $J=4$ (Imaginary part indicated in dashed line).

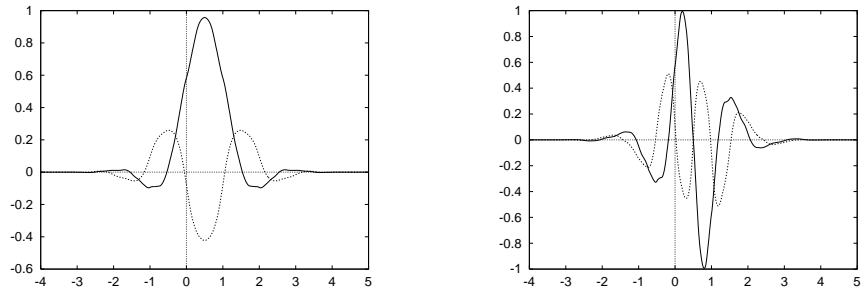


Figure 10: SDW4: scaling function (left) and wavelet (right) (Imaginary part indicated in dashed line).

6 The Phase of SDW Scaling Function

All Symmetric Daubechies Wavelets share the usual properties of the standard *real* Daubechies bases. This statement relies on the fact that most of those properties, which can be found either in [8] or [19], are based on the

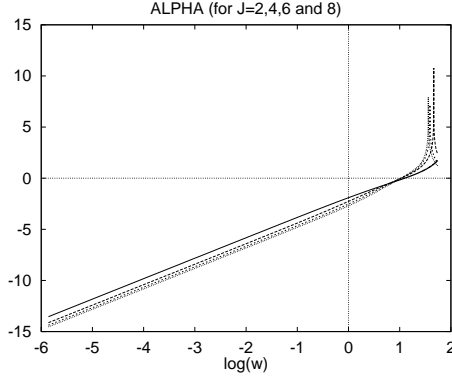


Figure 11: Left: $r(\omega)$; log-log scale. The slope of the straight lines is 2

modulus of the filters $m_0(\omega)$. Writing $\varphi(x) = h(x) + i g(x)$, we investigate the relationship between the real functions h and g .

Using the Fourier representation, we consider the ratio

$$r(w) = i \frac{\hat{g}(\omega)}{\hat{h}(\omega)} \quad (51)$$

This quantity is singular at $\omega = 2\pi$ and real-valued, because of the symmetry. On Fig.11, we plot the numerical computation of $r(\omega)$ in Log-Log scale for $J = 2, 4, 6$ and 8 . As seen on this figure, the complex scaling function is roughly approximated by the expression

$$\varphi(x) \simeq (1 + i\alpha \partial_x^2) h(x) \quad (52)$$

This approximation is accurately verified on the frequency domain defined by the sampling rate of the analysed signal. In other words, this identity is verified in the interval $[0, \pi]$ (with a sampling step renormalized to unity) when they are written in the Fourier representation.

For $J > 10$, higher derivative terms in $g(x)$ become non negligible. Let us note that $h(x)$ is further endowed with interesting vanishing moments:

$$\int dx h(x) = 1 \quad \text{and} \quad \int dx h(x) \left(x - \frac{1}{2}\right)^m = 0 \quad \text{for } m = 1, 2 \text{ and } 3 \quad (53)$$

In the early days of the Daubechies wavelets, the introduction of vanishing moments for the scaling function led to the construction of the well-known *coiflets*. The parameter α in Eq.(52) can be directly computed from the

filters coefficients a_k by using the first non vanishing momentum of $\varphi(x)$: writing

$$\gamma_i = \int \bar{\varphi}(x) x^i dx, \quad (54)$$

we have

$$\gamma_i = \frac{1}{2^i - 1} \sum_{j=0}^{i-1} m_{i-j} \gamma_j, \quad \text{with } m_k = \sum_{n=-J}^{J+1} n^k \bar{a}_n \quad \text{and } \gamma_0 = 1 \quad (55)$$

Straightforward integrations by part lead to

$$\alpha = -\frac{1}{2} \text{Im}(\gamma_2) \quad (56)$$

For $J = 2$ and 4 , α is respectively equal to -0.164 and -0.089 . We observe that Fig.7 and Fig.10 are consistent with Eq.(52). An other interesting rela-

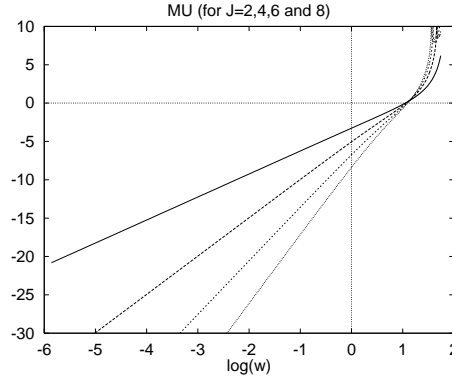


Figure 12: Left: $s(\omega)$; log-log scale. The slope of the straight lines are $J + 1$

relationship can be stated between ψ and φ . Writing $\psi(x) = w(x) + i v(x)$, we look at the relationship between the real functions w and h (the real part of the scaling function φ). As seen on Fig.12, it is found numerically that, at least for J up to 8, the ratio

$$s(w) = i \frac{\hat{w}(\omega)}{\hat{h}(\omega)} \quad (57)$$

is real and behave as w^{J+1} . Such a relationship certainly does not occur in the real Daubechies cases. However, it is worth recalling that continuous

wavelets are usually generated by taking successive derivatives of some scaling function as the Gaussian. The famous “mexican hat” wavelet is the second derivative of the Gaussian function. Here, we obtain compactly supported orthogonal complex wavelets whose real part is close to be the derivative of a smooth function, the real part of the corresponding complex scaling function.

7 The Mallat Algorithm with Complex filters

The discrete multiresolution analysis of f consists in the computation of the coefficients of the expansion

$$f(x) = \sum_k c_{j_0,k} \varphi_{j_0,k}(x) + \sum_{j=j_0}^{\infty} \sum_k d_{j,k} \psi_{j,k}(x) \quad (58)$$

where j_0 is a given scale (low resolution). In practice, the sum over j (the details at finest scales) is finite and f is projected onto some approximation space $V_{j_{max}}$:

$$P_{V_{j_{max}}} f(x) = \sum_k c_{j_{max},k} \varphi_{j_{max},k}(x) \quad (59)$$

The coefficients in the expansion (46) and (47) are computed through the orthogonal projection of the field over the multiresolution basis:

$$c_{j,k} = \langle \varphi_{j,k} | f \rangle, \quad d_{j,k} = \langle \psi_{j,k} | f \rangle \quad (60)$$

Starting with $P_{V_{j_{max}}} f$, the wavelet coefficients are computed with the *fast wavelet decomposition algorithm* \mathcal{W} composed with the low-pass projection $V_j \rightarrow V_{j-1}$ and the high-pass projection $V_j \rightarrow W_{j-1}$:

$$c_{j-1,n} = \sqrt{2} \sum_k \bar{a}_{k-2n} c_{j,k}, \quad \text{and} \quad d_{j-1,n} = \sqrt{2} \sum_k \bar{b}_{k-2n} c_{j,k} \quad (61)$$

Conversely, any elements of V_{j-1} and of W_{j-1} can combine to give a unique vector in V_j ; this reconstruction (denoted by \mathcal{W}^{-1}) is expressed by the inverse fast wavelet transform:

$$c_{j,n} = \sqrt{2} \sum_k a_{n-2k} c_{j-1,k} + \sqrt{2} \sum_k b_{n-2k} d_{j-1,k} \quad (62)$$

In most applications, the signal to be analyzed is real-valued: the complex wavelet representation provides a redundant description of the signal.

Eq.(52) helps in interpreting this redundancy since, using the Taylor expansion of a one dimensional field, we can estimate the real and imaginary parts of the coefficients c_k^j as

$$\begin{cases} Re(c_{j,k}) \simeq 2^{\frac{-j}{2}} f(x_{j,k}) \\ Im(c_{j,k}) \simeq \frac{\alpha}{2^{\frac{3}{2}j+1}} f''(x_{j,k}) \end{cases} \quad \text{with } x_{j,k} = \frac{2k+1}{2^{j+1}}. \quad (63)$$

Let us consider the estimate of the finest scale approximation of f , i.e $P_{V_{j_{max}}}(f)$, given a sampled function f_k . A crude approximation is simply given by $c_{j_{max},k} = 2^{\frac{-j}{2}} f_k$. Denoting by $\mathfrak{R}_j \subset V_j$ the set of all functions in V_j with real valued modes; this approximation is nothing but the orthogonal projection (denoted by $P_{\mathfrak{R}_{j_{max}}}$) of f onto $\mathfrak{R}_{j_{max}}$. This corresponds to the ‘‘Mallat’s initial conditions’’ for the fast wavelet transform. A more accurate estimate of $P_{V_{j_{max}}}(f)$ is obtained by using the operator

$$P_{V_{j_{max}}} \approx \mathcal{W} P_{\mathfrak{R}_{j_{max}+1}} \mathcal{W}^{-1} P_{\mathfrak{R}_{j_{max}}} \quad (64)$$

This projection gives a non trivial imaginary part for the $c_k^{j_{max}}$. As expected, it corresponds to the Laplacian of the estimated real part. This is illustrated nicely in the 2d example displayed in Fig.13.

8 Restoration from the Phase

The issue discussed here is to understand the redundancy of the complex wavelet representation of a real signal. In other words, we want to understand the ‘‘role of the phase of a complex wavelet coefficient $d_{j,k}$. For simplicity of notation, the discussion is done for 1d signals but the simulation is presented in two dimensions.

Let us first define two projectors, $P_{\mathfrak{R}}$ and P_{Γ} . The projector $P_{\mathfrak{R}}$ extracts the first order approximation of the scaling coefficient of the expansion (59) at the finest resolution (\mathfrak{R} denotes the real part):

$$P_{\mathfrak{R}}(c_{j_{max},k}) = \mathfrak{R}(c_{j_{max},k}) \quad (65)$$

Let us now consider the wavelet expansion (58) of a given field f_0 and define the phase of the wavelet coefficients $\theta_{j,k} = Arg(d_{j,k})$. We observe that the new set of functions $\Psi_{j,k}(x) = e^{i\theta_k^j} \psi_{j,k}(x)$ is also an orthonormal basis of



Figure 13: Projection onto $V_{j_{max}}$: real part (left) and imaginary part (right) of $P_{V_{j_{max}}} I$. (The original image is the right image displayed on Fig.19).

$L^2(\mathbb{R})$: this “local rotation” of the wavelet basis leads to a multiwavelet basis adapted to the signal. Indeed, we define the *isophase space* Γ by the set of all expansions

$$\sum_k \langle \varphi_{j,k} | f_0 \rangle \varphi_{j_0,k}(x) + \sum_{j=j_0}^{j_{max}-1} \sum_k r_{j,k} \Psi_{j,k}(x) \quad (66)$$

where the coefficients r_k^j are now positive real numbers. P_Γ is the orthogonal projector on this space that depends on the the phase of the wavelet coefficients of the original field we start with. Given an arbitrary wavelet expansion of the form (2) with $d_{j,k} = w_{j,k} + i v_{j,k}$, the projection on the isophase space is defined by the closest point on Γ , i.e.

$$P_\Gamma f = \sum_k \langle \varphi_{j,k} | f_0 \rangle \varphi_{j_0,k} + \sum_{j=j_0}^{j_{max}-1} \sum_k r_{j,k} \Psi_{j,k} \quad (67)$$

with

$$r_{j,k} = \begin{cases} 0, & \text{if } \cos \theta_{j,k} w_{j,k} + \sin \theta_{j,k} v_{j,k} < 0 \\ \cos \theta_{j,k} w_{j,k} + \sin \theta_{j,k} v_{j,k} & \text{otherwise} \end{cases} \quad (68)$$

We further observe that both $P_{\mathfrak{R}}$ and P_Γ project onto convex spaces (POCS). Considering an arbitrary point \tilde{f}_0 in Γ , a well-known theorem states that the

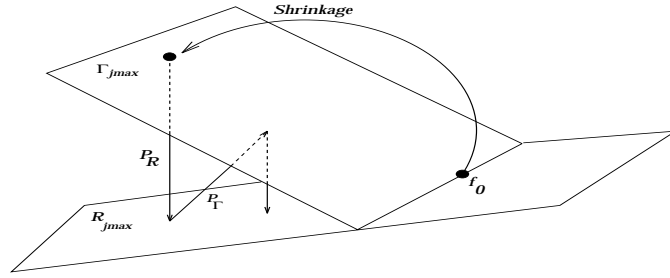


Figure 14: Phase reconstruction by alternating projections on affine spaces $\Gamma_{j_{max}}$ and $R_{j_{max}}$

sequence of alternate projections

$$f_n = (P_{\mathbb{R}}P_{\Gamma})^n P_{\mathbb{R}}(\tilde{f}_0) \quad (69)$$

converges and, in the present case, the limit point is the original real signal f_0 from which we defined Γ .

The two-dimension generalization of this algorithm is straightforward using the usual cross-product of the 1-d multiresolution basis. For the sake of illustration of the “phase reconstruction algorithm”, Fig.15 displays the original picture f_0 , the initial point $P_{\mathbb{R}}\tilde{f}_0$ (obtained by killing all the modulus of the wavelet coefficients of the four-level decomposition *i.e.* $j_0 = j_{max} - 4$ with SDW $J = 2$) and the POCS reconstructions $f_{n=100}$ and $f_{n=1000}$. We first

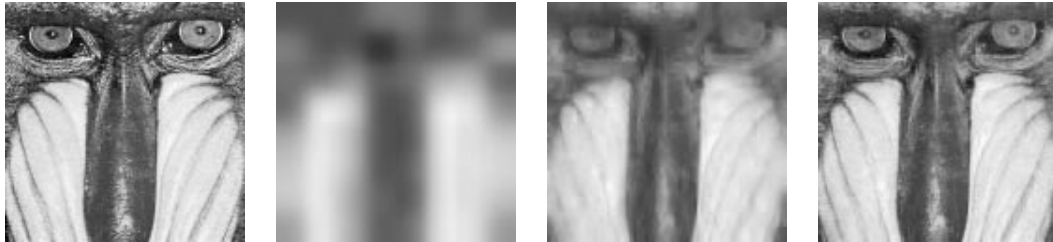


Figure 15: From left to right: f_0 , $P_{\mathbb{R}}\tilde{f}_0$, f_{100} and f_{1000}

notice that the POCS gradually restores the details of the image from coarse

to fine. As we can notice in Eq.(68), the projector P_Γ “shrinks” the modulus of the wavelet coefficients, even to 0. It is worth recalling that shrinkage techniques are nowadays an efficient tool for denoising. Phases thus encode the “coherent” structures of the signal and the POCS algorithm reconstructs the original image through the coherency of the encoded information. The restoration of the modulus of the wavelet coefficients is illustrated in Fig.17: coefficients of the coarser level $j = j_0 = j_{max} - 4$ and those of the finest scale $j = j_{max} - 1$, both for $f_{n=1000}$. We can observe the resulting shrinkage of the wavelet coefficients that depends on the scale of the details. Let us

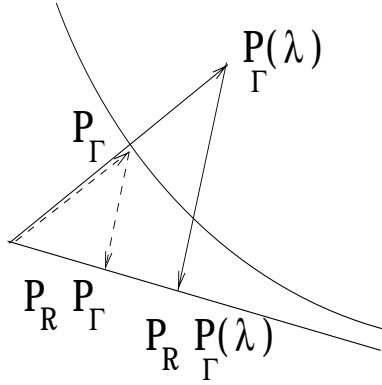


Figure 16: Phase reconstruction by alternating projections with relaxation parameter λ

further mention the significant speed-up of the POCS algorithm by using a relaxation parameter in the isophase projector. This is done by redefining P_Γ as follows

$$P_\Gamma(\lambda) = (1 - \lambda) + \lambda P_\Gamma. \quad (70)$$

In place of Eq.(69), we now consider the new sequence of projections (see Fig.16)

$$f_n = (P_{\Re} P_\Gamma(\lambda_n))^n P_{\Re}(\tilde{f}_0) \quad (71)$$

where λ_n is computed in order to minimize the quadratic error $\|f_n - f\|^2$. The iterative algorithm is obtained on the form

$$f_{n+1} = P_{\Re} P_\Gamma f_n + \delta_n (P_{\Re} P_\Gamma f_n - f_n) \quad (72)$$

with $\delta_n = \frac{d_n}{r_n}$, where d_n is the distance between the two convex (i.e. the energy of the imaginary part killed in the projection P_{\Re}),

$$d_n = \|P_{\Re}P_{\Gamma}f_n - P_{\Gamma}f_n\|^2 \quad (73)$$

and r_n is given by

$$r_n = \|P_{\Re}P_{\Gamma}f_n - f_n\|^2 \quad (74)$$

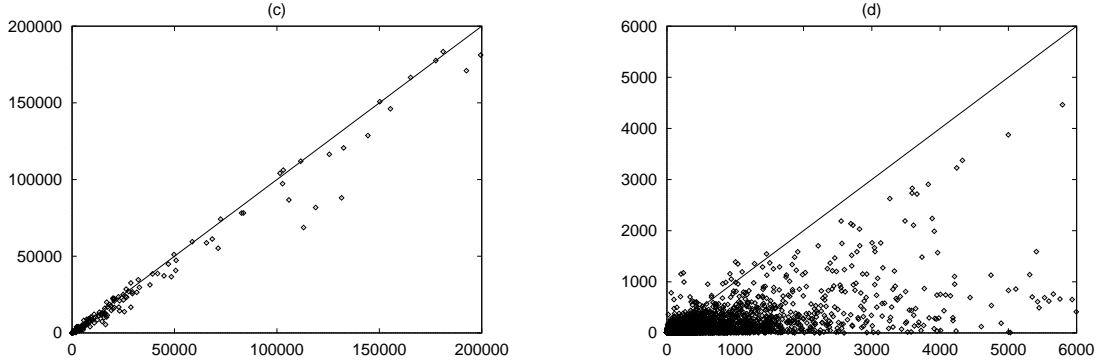


Figure 17: Left: coarse scale wavelet modulus of f_{1000} vs. original wavelet modulus; Right: finest scale wavelet modulus of f_{1000} vs. original wavelet modulus.

9 Image Enhancement

The bi-dimensional multiresolution analysis is built from the product of two multiresolution spaces V_i . The scaling function $\Phi(x, y) = \varphi(x)\varphi(y)$ generates V_0 and, complemented with three wavelets $\Psi^0(x, y) = \psi(x)\psi(y)$, $\Psi^1(x, y) = \psi(x)\varphi(y)$, $\Psi^2(x, y) = \varphi(x)\psi(y)$, it spans V_1 . The functions are complex-valued. In particular, we have

$$\Phi(x, y) = \Theta(x, y) + i \Psi(x, y) \quad (75)$$

and expansion [58] or [59] now generalize in two dimensions as

$$\begin{aligned}
P_{V_{j_{max}}} I(x, y) &= \sum_{m,n} c_{j_{max},m,n} \Phi_{j_{max},m,n}(x, y) \\
&= \sum_{k_1,k_2} c_{j_0,k_1,k_2} \Phi_{j_0,k_1,k_2}(x, y) \\
&+ \sum_{i=0}^2 \sum_{j=j_0}^{j_{max}-1} \sum_{k_1,k_2} d_{j,k_1,k_2}^i \Psi_{j,k_1,k_2}^i(x, y)
\end{aligned} \tag{76}$$

where

$$\Phi_{j,k_1,k_2}(x, y) = 2^j \Phi(2^j x - k_1, 2^j y - k_2) \tag{77}$$

and

$$\Psi_{j,k_1,k_2}^i(x, y) = 2^j \Psi^i(2^j x - k_1, 2^j y - k_2) \tag{78}$$

span the spaces V_j and W_j^i respectively so that

$$V_{j+1} = V_j \oplus W_j^0 \oplus W_j^1 \oplus W_j^2. \tag{79}$$

In the sequel, we denote by \mathcal{W}^N the N-levels wavelet transform

$$\{c_{m,n}^{j_{max}}\} \xrightarrow{\mathcal{W}^N} \{c_{m,n}^{j_{max}-N}, \mathbf{d}_{j_{max}-N,m,n}, \mathbf{d}_{j_{max}-2,m,n}, \dots, \mathbf{d}_{j_{max}-1,m,n}\} \tag{80}$$

where $\mathbf{d} = (d^0, d^1, d^2)$. Fig.13 shows an example of the projection $P_{V_{j_{max}}} I$ and Fig.18 displays the modulus of the complex wavelet coefficients (and the $c_{k_1,k_2}^{j_0}$'s in the upper left corner). The real and imaginary parts of the scaling function are

$$\begin{cases} \Theta(x, y) = h(x)h(y) - g(x)g(y) \simeq G(x, y) \\ \Psi(x, y) = h(x)g(y) + g(x)h(y) \simeq \alpha \Delta G(x, y) \end{cases} \tag{81}$$

where $G(x, y)$ denotes the real smoothing kernel $h(x)h(y)$. On one hand, the real part of the 2-d scaling function is close (because $\alpha^2 \ll 1$) to the smoothing kernel $G(x, y)$ while, on the other hand, the imaginary part is proportional to the Laplacian of $G(x, y)$: $\Psi(x, y)$ is thus the ‘‘Marr wavelet’’ associated with $\Theta(x, y) \simeq G(x, y)$.

Since the real and imaginary parts of the wavelet transform coefficients of some *real* image correspond to the convolution of the original field with the

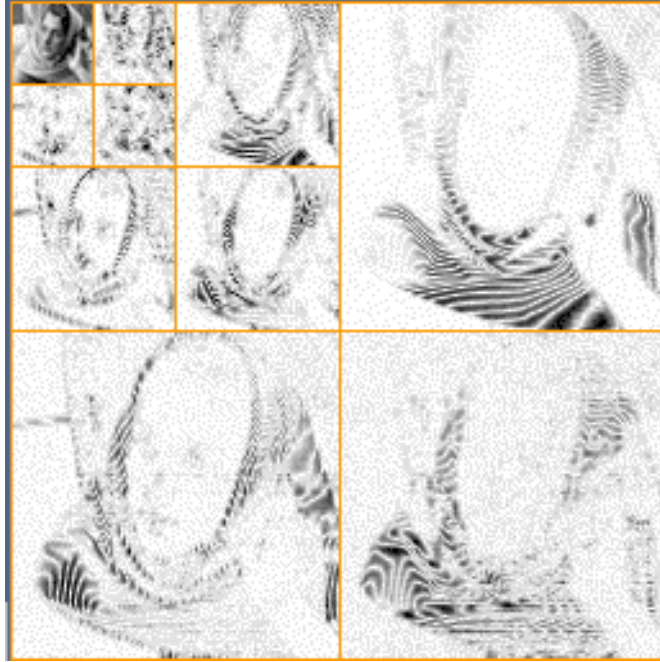


Figure 18: Modulus of the complex wavelet coefficients (SDW4, N=3). The top left sector is the matrix of coefficients $c_{m,n}^{j_0}$. The other sparse matrices are the wavelets coefficients when the scale j increases from j_0 to $j_{max} = j_0 + 3$ (3 directional wavelets).

real part and the imaginary part of $\Phi_{j,m,n}(x, y)$ respectively, we then have access to the (multiscaled) smoothed Laplacian of the image:

$$\begin{cases} h_{k_1, k_2}^j = \text{Re}(c_{k_1, k_2}^j) = 2^j I(x, y) * G(2^j x - k_1, 2^j y - k_2) \\ g_{k_1, k_2}^j = \text{Im}(c_{k_1, k_2}^j) = -\frac{\alpha}{2^j} \Delta I(x, y) * G(2^j x - k_1, 2^j y - k_2) \end{cases} \quad (82)$$

The simultaneous presence of a smoothing kernel and its Laplacian in the complex scaling function can be exploited to define some elementary operations on the wavelet coefficients. In other words, we use this information to synthetise a *new* image that corresponds to some prescribed operation. A typical example is de-noising; this application is among the most succesful applications of wavelets. Here, we investigate the *edge enhancement* that is

usually implemented through the sharpening operator

$$I \rightarrow \tilde{I} = I - \rho \Delta I \quad (83)$$

Starting with an expansion of the form given by Eq.(76), we synthesize a new image

$$\tilde{I} = I_0 + \sum_{l=j_0}^{j_{max}-1} D_l \quad (84)$$

defined by

$$I_0(x, y) = \sum_{m,n} c_{j_0,m,n} \Phi_{j_0,m,n}(x, y) \quad (85)$$

$$D_l(x, y) = \lambda_l \sum_{k_1,k_2} g_{l,k_1,k_2} \Phi_{l,k_1,k_2}(x, y) + \sum_{\iota=0}^2 \sum_{k_1,k_2} \delta_l(d_{l,k_1,k_2}^\iota) \Psi_{l,k_1,k_2}^\iota(x, y) \quad (86)$$

where the scale l runs from j_{max} to the coarse scale j_0 . λ_l are real valued and $\delta_l(z)$ are some functions of the complex wavelet coefficients. Our intention is to extract various kind of details at different dyadic scales of the image and to add them to the original with appropriate weights. Some particular choice of λ_l 's and δ_l 's are particularly worth to mention. For example, let us consider:

$$\begin{cases} \lambda_l \geq 0, \\ \delta_l(d) = (1 + \epsilon_l)d, \end{cases} \quad (87)$$

We observe that $\lambda_l = \epsilon_l = 0$ leads to the identity, *i.e* $I = \tilde{I}$. Introduction of non vanishing (but small) λ_l amounts to add scale dependent details that are similar to the multiscale laplacian.

Figure 19 shows an example of such a processing with *SDW4* and $N = 3$. In comparison with the original image, the local contrast has been improved significantly: artefacts from the scanner acquisition are now apparent in the processed lady image. This ‘‘anomaly detection’’ is one of the most promising applications of multiscale representations. Let us mention that other efficient multiscale sharpening transformations have been proposed in the recent past. The main difference in the present work is the orthogonality property of the SDW transform and the use of the phase of a complex basis. We recall that the SDW bases are not derived from a representation that allows specific enhancements. On the contrary, the Laplacian has been shown to be inherent to this particular orthogonal basis.



Figure 19: Image Enhancement: The test image at left. The right image has been synthesized using non vanishing λ 's and ϵ in Eq.(80) and Eq.(82)

10 Complex Shrinkage

Let us now consider an image corrupted with additive Gaussian noise (denoted by N) projected into the approximation space of highest resolution

$$\tilde{I}(x, y) = \sum_{m,n} \tilde{c}_{j_{max},m,n} \Phi_{j_{max},m,n}(x, y) \quad (88)$$

We want to estimate a real signal

$$I_0(x, y) = \sum_{m,n} C_{j_{max},m,n} \Phi_{j_{max},m,n}(x, y) \quad (89)$$

from the observed image $\tilde{I} = I_0 + N$. The wavelet shrinkage technique amounts to computing estimates from the wavelet representation of the observed signal. Let

$$I(x, y) = \sum_{k_1, k_2} \tilde{c}_{k_1, k_2} \Phi(x - k_1, y - k_2) + \sum_{\iota=0}^2 \sum_{j=0}^{j_{max}-1} \sum_{k_1, k_2} d_{j, k_1, k_2}^{\iota} \Psi_{j, k_1, k_2}^{\iota}(x, y). \quad (90)$$

We have to solve the following variational problem: given a positive Lagrange parameter λ , find an image I^* that minimizes the functional

$$\mathcal{L}(I) \stackrel{\text{def}}{=} E(\tilde{I}, I) + \lambda S(I). \quad (91)$$

Here $E(\tilde{I}, I)$ is the root-mean square error between the observed and test images:

$$E(\tilde{I}, I) = \|I - \tilde{I}\|^2 = \sum_{\iota=0}^2 \sum_{j=0}^{j_{max}-1} \sum_{k_1, k_2} |d_{j, k_1, k_2}^\iota - \tilde{d}_{j, k_1, k_2}^\iota|^2, \quad (92)$$

whereas $S(I)$ represents some constraint on the regularity of the optimal solution; in fact it regularizes the ill-posed problem of minimizing E alone. The choice of this constraint involves some *a priori* knowledge about the *true* signal we aim to restore. The parameter λ controls the trade-off between goodness of fit and *a priori* smoothness. This latter property, given by $S(I)$, can be quantified by using a norm in some Besov space (see Ref.[9]). An important result in wavelet theory is the definition of such a norm in the wavelet representation. Considering the Besov space $B_{p,q}^\alpha$ (i.e. the space of functions “with α derivatives in L_p ”), it can be shown that

$$S(I) = \sum_{\iota=0}^2 \sum_{j=0}^{j_{max}-1} 2^{js'p} \left(\sum_{k_1, k_2} |d_{j, k_1, k_2}^\iota|^p \right)^{\frac{q}{p}}, \quad s' = \alpha + 1 - \frac{2}{p} \quad (93)$$

defines a norm in this space. For the sake of simplicity, we consider here $p = q = 1$ and $\alpha = 1$; then

$$S(I) = \sum_{\iota=0}^2 \sum_{j=0}^{j_{max}-1} \sum_{k_1, k_2} |d_{j, k_1, k_2}^\iota| \quad (94)$$

and the functional defined in Eq.(91) can be read as

$$\mathcal{L}(I) = \sum_{\iota=0}^2 \sum_{j=0}^{j_{max}-1} \sum_{k_1, k_2} \mathcal{F}(d_{j, k_1, k_2}^\iota, \tilde{d}_{j, k_1, k_2}^\iota) \quad (95)$$

with

$$\mathcal{F}(d, \tilde{d}) = |\tilde{d} - d|^2 + \lambda |d|. \quad (96)$$

Equation (94) illustrates the efficiency of the wavelet representation for solving the above optimization problem since it “diagonalizes” the functional over

each coefficient of the decomposition. As illustrated on Fig.20, the solution d^* of our variational problem,

$$d^* = \text{Argmin } \mathcal{F}(d, \tilde{d}) \quad (97)$$

is clearly a point lying on the ray defined by the phase of \tilde{d} . In other words, the phase is preserved and plays a role in this problem rather like a parameter. Let us re-write $\mathcal{F}(d, \tilde{d})$ in terms of the amplitudes,

$$\mathcal{F}(r, \tilde{r}) = (\tilde{r} - r)^2 + \lambda r \quad (98)$$

The solution of $\text{Argmin } \mathcal{F}(r, \tilde{r})$ is obviously given by

$$r^* = \left(r - \frac{\lambda}{2}\right)_+ \quad (99)$$

where $(x)_+$ is equal to x for $x \geq 0$ and 0 elsewhere (see dashed line on Fig.21). We thus obtain a soft-shrinkage of the wavelet coefficients amplitude with a threshold defined by $\lambda(j)$. Denoting by \mathcal{T} this shrinkage operator of the wavelet coefficients, the resulting estimate is given by

$$I^* = (\mathcal{W}^{-1} \mathcal{T} \mathcal{W}) \tilde{I} \quad (100)$$

Let us emphasize that this approximation is obtained by modifying only the amplitude of the wavelet coefficients: the phases are preserved. This fact will be explicitly used in the Bayesian approach considered in the sequel. Let us consider the general case of a zero-mean complex Gaussian random variable η with a normal distribution (see for instance Ref.[20]). Following the recent work of Picinbono [21], we define the variance σ^2 and the ‘‘relation’’ C by

$$\sigma^2 \stackrel{\text{def}}{=} E(\eta\bar{\eta}), \quad C \stackrel{\text{def}}{=} E(\eta^2) \quad (101)$$

The complex Gaussian distribution is then described by the density function

$$p(\eta, \bar{\eta}) = \frac{1}{\sigma^2 \pi} \frac{1}{\sqrt{1 - \rho^2}} e^{-\frac{1}{2}Q(\eta, \bar{\eta})} \quad (102)$$

with

$$Q(\eta, \bar{\eta}) = (\eta, \bar{\eta}) \begin{pmatrix} \sigma^2 & C \\ \bar{C} & \sigma^2 \end{pmatrix}^{-1} \begin{pmatrix} \eta \\ \bar{\eta} \end{pmatrix} \quad \text{and} \quad C = \sigma^2 \rho e^{i\gamma}. \quad (103)$$

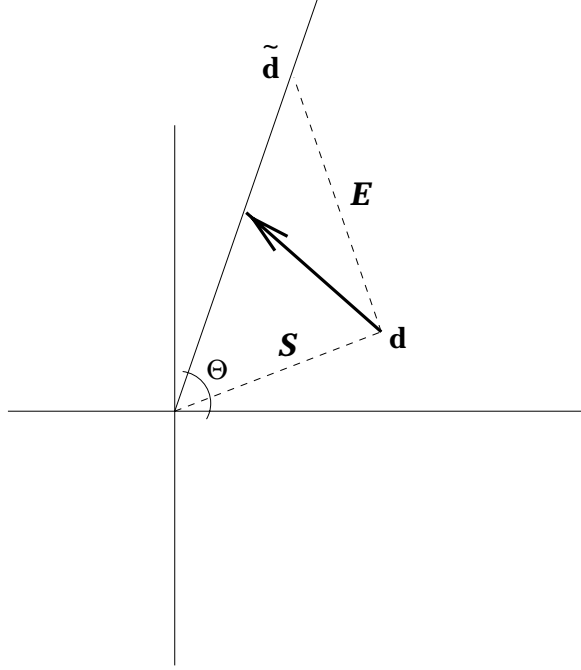


Figure 20: Solution of $\text{Argmin } \mathcal{F}(d, \tilde{d})$

Straightforward computation yields the following expression for Q :

$$Q(\eta, \bar{\eta}) = 2|\eta|^2 \frac{1 - \rho \cos(2\text{Arg}\eta - \gamma)}{\sigma^2(1 - \rho^2)} = 2 \frac{\epsilon^2}{\sigma^2 \Gamma(\alpha)} \quad (104)$$

where $\eta = \epsilon e^{i\alpha}$ and

$$\Gamma(\alpha) = \frac{(1 - \rho^2)}{1 - \rho \cos(2\alpha - \gamma)} \quad (105)$$

Let us consider the following expression for the wavelet coefficients computed from the observed image \tilde{I} (we omit to write the indices j, k):

$$\tilde{d} = d_0 + \eta, \quad \text{i.e.} \quad \epsilon e^{i\alpha} = r e^{i\theta} - \mu e^{i\zeta} \quad (106)$$

using the polar representation of the wavelet coefficients, $\tilde{d} = r e^{i\theta}$ and $d_0 = \mu e^{i\zeta}$. First we obtain the following likelihood function:

$$\pi(r, \theta | \mu, \zeta; \sigma, \rho, \gamma, \alpha) \sim r e^{-\frac{(r-\mu)^2 - 2r\mu(1 - \cos(\theta - \zeta))}{\sigma^2 \Gamma(\alpha)}} \quad (107)$$

Second, since we are interested in an estimator that preserves the phase of the wavelet coefficient, *i.e.* an estimator of the amplitude only, we define a likelihood on the amplitude $r_{j,k}$ by

$$\Pi_{j,k}(r|\mu) = \pi(r, \theta = \theta_{j,k} | \mu, \zeta = \theta_{j,k}, \sigma, \rho, \gamma, \alpha = \theta_{j,k}) \sim r e^{-\frac{(r-\mu)^2}{\sigma^2 \Gamma(\theta_{j,k})}} \quad (108)$$

Let us comment on the various “hidden” parameters (assumed to be known) in $\Gamma(\theta_{j,k})$. The angle $\frac{1}{2}\gamma$ defines the principal axis of the distribution (for the noise) in the complex plane; the ρ parameter takes real values between 0 and 1 and measures the “circularity” of the complex noise component (see [21]): if the data are circular (*i.e.* the phases are meaningless), then $\rho \sim 0$; however, real and imaginary parts are strongly correlated for $\rho \sim 1$ (the limiting case $\rho = 1$ is obtained with the Haar wavelet for which all the wavelet coefficients lie on a line). The variance σ intuitively measures the noise level. In a fully Bayesian analysis, it would be possible to assume prior distributions on each of these parameters in Eq.(107). Here, however, we perform a partial Bayesian analysis by first using the wavelet coefficients at the finest scale to estimate Γ, ρ and γ and also using the fact that $\alpha = \zeta = \theta_{j,k}$. Thus, the following estimators of the parameters arise naturally:

$$\sigma^2 = \text{E}[\tilde{d}_{j_{max},k} \tilde{d}_{j_{max},k}^*] \quad (109)$$

$$\rho e^{i\gamma} = \frac{1}{\sigma^2} \text{E}[\tilde{d}_{j_{max},k}^2] \quad (110)$$

Following the previous discussion, the prior distribution on μ , which can be considered as a measure of smoothness, should depend on the Lagrange parameter λ in Eq.[91]. Here, we choose to model this smoothness by a Gamma($2, \frac{1}{\lambda}$) density; that is

$$\pi(\mu) \sim \mu e^{-\lambda\mu}. \quad (111)$$

The resulting posterior density for μ is thus found to be

$$\Pi_{j,k}(\mu|r) = \frac{\mu e^{-\frac{(r-\mu)^2}{\sigma^2 \Gamma(\theta_{j,k})} - \lambda\mu}}{\int_0^\infty r' e^{-\frac{(r-r')^2}{\sigma^2 \Gamma(\theta_{j,k})} - \lambda r'} dr'} \quad (112)$$

The Bayes estimate can now be specified as follows. Let us consider the signal contaminated by additive noise and expanded in some orthogonal discrete wavelet basis. The Bayes estimator with respect to the quadratic loss

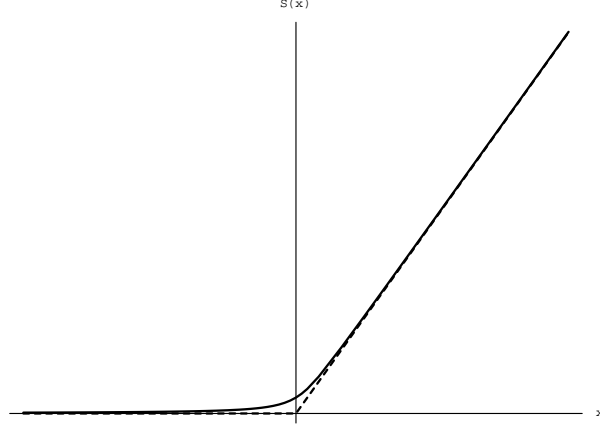


Figure 21: Shrinkage function $\mathcal{S}(x)$

of the wavelet coefficient amplitude is equal to the mean of the posterior distribution: that is, for any pair of indices (j, k) , the Bayesian estimator $\delta_{j,k}(r)$ of the amplitude of wavelet coefficient $d_{j,k}$, given the observed amplitude $r = r_{j,k}$ is

$$\delta_{j,k}(r) = \int_0^\infty \mu \Pi_{j,k}(\mu|r) d\mu = \frac{\int_0^\infty r'^2 e^{-\frac{(r-r')^2}{\sigma^2\Gamma(\theta_{j,k})} - \lambda r'} dr'}{\int_0^\infty r' e^{-\frac{(r-r')^2}{\sigma^2\Gamma(\theta_{j,k})} - \lambda r'} dr'} \quad (113)$$

Using the following probability integral[2],

$$\int_0^\infty x^n e^{-\frac{1}{2}x^2 - zx} dx = n! \sqrt{2^{n-1}\pi} \text{i}^n \text{erfc}\left(\frac{-z}{\sqrt{2}}\right) \quad (114)$$

where $\text{i}^n \text{erfc}(x)$ denotes the repeated integrals of the Error function:

$$\text{i}^n \text{erfc}(z) = \int_z^\infty \text{i}^{n-1} \text{erfc}(x) dx, \quad \text{i}^0 \text{erfc}(z) = \text{erfc}(z) \quad (115)$$

we obtain the following expression for the estimator

$$\delta_{j,k}(r) = \sigma \sqrt{\frac{\Gamma(\theta_{j,k})}{2}} \mathcal{S}\left(\frac{1}{\sigma} \sqrt{\frac{2}{\Gamma(\theta_{j,k})}} \left(r - \frac{\lambda(\theta_{j,k})}{2}\right)\right) \quad (116)$$

with

$$\lambda(\theta) = \lambda \sigma^2 \Gamma(\theta) \quad (117)$$

and

$$\mathcal{S}(x) = x + \frac{1}{\sqrt{2}} \frac{\operatorname{erfc}\left(\frac{-x}{\sqrt{2}}\right)}{\operatorname{ierfc}\left(\frac{-x}{\sqrt{2}}\right)} \quad (118)$$

As seen on the graph of the Fig.22, $\mathcal{S}(x)$ gives a “supersmooth” version of a “soft-shrinkage” estimator. This function and the phase-dependent estimator given by Eq.(116) are our main results. In Fig.22, we show the phase dependency of the threshold for various values of the “circularity”. As expected, we observe that the limiting case $\rho \approx 1$ does correspond to the usual real case for which a single phase (e.g 0 or π) is present in the decomposition. Conversely, the threshold does not depend on the phase when the data are circular, i.e when $\rho \approx 0$. Note that approximating $\mathcal{S}(x)$ by $(x)_+$ (the dashed line on Fig.21) simplifies the result in Eq.(116) and leads to the estimator

$$\delta_{j,k}(r) = \left(r - \frac{\lambda(\theta_{j,k})}{2}\right)_+ \quad (119)$$

As expected, this result extend the initial estimate (99) with an explicit dependence on the phase. Images displayed in Fig.23 illustrate the technique presented here. In the upper and lower images both columns contain the noisy observed images and the corresponding estimates respectively. It should be mentioned that we have used $\lambda = \sqrt{2 \ln n} \sigma^{-1}$ in Eq.(116) (n being the number of pixels of the image) in order to recover the universal threshold of Ref.[10] when $\rho = 1$.

11 Conclusion

Ten years after the celebrated work of I. Daubechies [7] (finding the compactly supported wavelets orthonormal bases with maximum number of vanishing moments), the present paper describes a generalization of this problem,

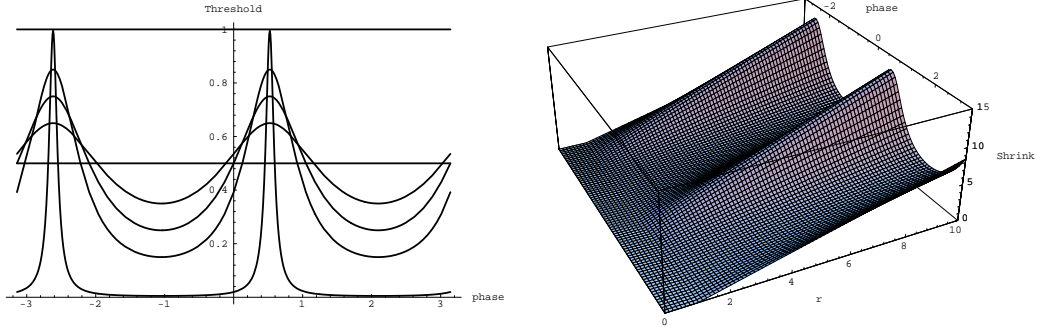


Figure 22: Left: Plots of $0.5\Gamma(\theta)$, for various values of ρ . (The threshold is flat for $\rho = 0$ and peaky for $\rho \approx 1$). Right: $\delta_{j,k}(r)$.

pointing out the existence of symmetric solutions. Indeed, such solutions are complex-valued and exhibit extra-properties that have been used in various applications, mainly in image processing. Presently, Wavelet-based processing has reached a mid-term maturity and only few methods have taken advantage of this new framework for the signals description. All of these applications make use of statistical analysis of signals: zero-tree coding and data compression, de-noising, multiscale modeling,... One of the most interesting and significant applications of this technique has been in the field of medical image processing, where it has helped interpret signals. In Fig.24, we illustrate this with a mammogram in which details as small as the microcalcifications have been amplified using the approach described in Section 9 where we use the complex nature of our solutions. Indeed, in Section 6, we explain the presence of a wavelet in the imaginary part of the scaling function: the sharpening enhancement illustrated in Fig.24 is mainly based on this result. The phase of the solutions has also been useful in the de-noising application presented in Section 10. It is worth comparing our approach with the multi-wavelet shrinkage method proposed by the authors of [11]. The complex solutions $\varphi(x) = h(x) + i g(x)$, $\psi(x) = w(x) + i v(x)$, can be trivially

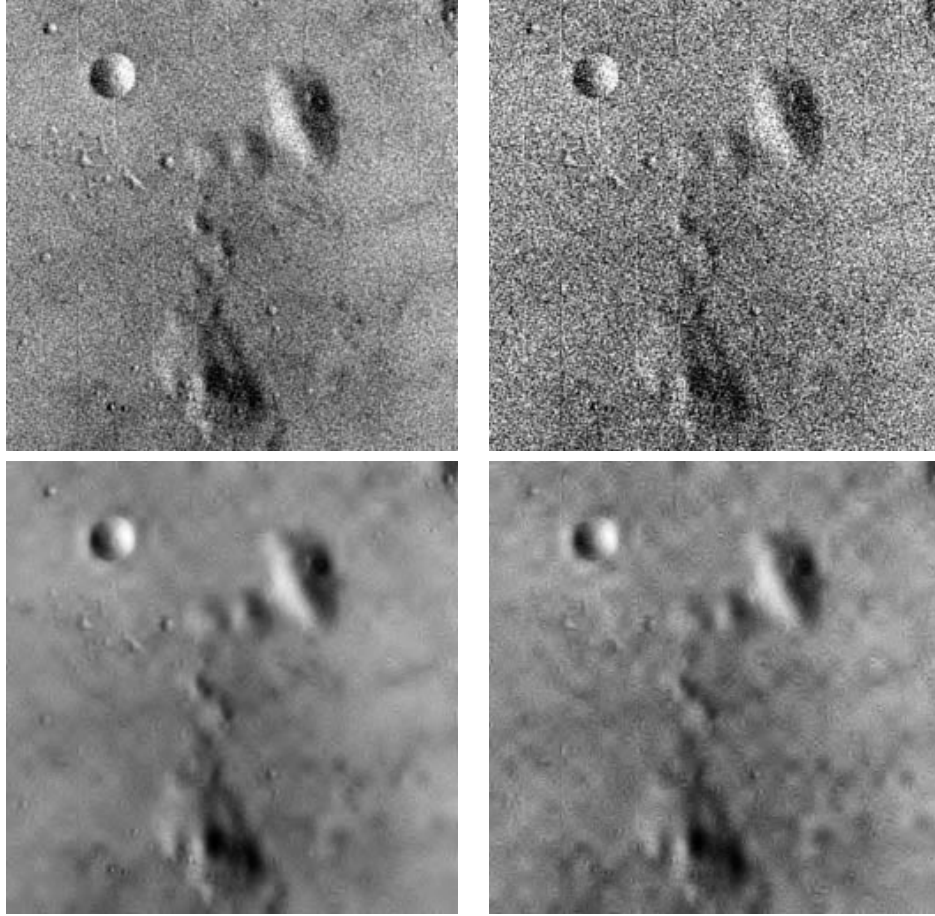


Figure 23: Noisy and estimated images

recast as real-valued multi-wavelet solutions where we consider vectors

$$\Phi(x) = \begin{pmatrix} h(x) \\ g(x) \end{pmatrix}, \quad \Psi(x) = \begin{pmatrix} w(x) \\ v(x) \end{pmatrix} \quad (120)$$

and the matrix form of equations (12) and (23). In this framework, a multivariate statistical analysis of the 2d-wavelet coefficients has been carried out in [11] and an “ellipsoidal” shrinkage has been proposed. This estimator amounts to preserving what we unambiguously identified as the phase of the complex wavelet coefficients. Moreover, we justified preserving the phases in Section 10. Let us mention that such “ellipsoidal” shrinkage technique has

been used efficiently in the complex framework by the authors of [12]. Their estimator corresponds to our result (119). They have shown, with careful comparisons, that this de-noising technique based on complex wavelets outperformed the other standard methods for reducing speckle artefacts in SAR images.

Acknowledgements. This work is supported in part by A.N.S. Technologies Ltd. (Montreal, Canada) and by the Natural Sciences and Engineering Research Council (NSERC) of Canada.

References

- [1] F. Abramovich, T. Sapatinas and B.W. Silverman, Wavelet thresholding via a Bayesian approach, Tech. Report, School of Mathematics, Univ. of Bristol (UK), 1996.
- [2] M. Abramowitz and I. Stegun, *Handbook of Mathematical Functions*, NBS Applied Math. Series, 1964.
- [3] G. Battle, A block spin construction of ondelettes. Part I: Lemarié functions, *Comm. Math. Phys.*, 110, p.601, 1987.
- [4] B. Belzer, J-M. Lina and J. Villasenor, Efficient Image Compression using Complex Wavelets filters, *IEEE Trans. on Signal Processing*, vol. 43, 10, p.2425, 1995.
- [5] H.A. Chipman, E.D Kolaczyk and R.E. McCulloch, Adaptive Bayesian wavelet shrinkage, Tech. Report 421, Dep. of Statistics, Univ. of Chicago, 1996.
- [6] M. Clyde, G. Parmigiani and B. Vidakovic, Multiple shrinkage and subset selection in wavelets. Discussion Paper 95-37, ISDS, Duke Univ., 1995.
- [7] I. Daubechies, *Orthonormal bases of compactly supported Wavelets*, *Commun. on Pure and Appl. Math.*, 41, p.909, 1988.
- [8] I. Daubechies, *Ten Lectures on Wavelets*, S.I.A.M., Philadelphia, 1992.

- [9] R. De Vore and B. J. Lucier, Fast wavelet techniques for near-optimal image processing, Proc. 1992 IEEE Military Commun. Conf., IEEE Communications Soc., NY 1992.
- [10] D. Donoho and I. Johnstone, Wavelet shrinkage: Asymptopia?, *J. R. Statist. Soc. B*, p. 301, 1995 (and reference therein).
- [11] T.R. Downie and B.W. Silverman, The discrete multiple wavelet transform and the thresholding methods, Tech. Report, School of Mathematics, Univ. of Bristol (UK), 1996.
- [12] L. Gagnon and F. Drissi Smaili, Speckle noise reduction of airborne SAR images with symmetric Daubechies wavelets, SPIE-2759, 1996.
- [13] W. Lawton, Applications of Complex Valued Wavelet Transforms to Subband Decomposition, IEEE Trans. on Signal Proc., vol.41, p.3566, 1993.
- [14] J.M. Lina and M. Mayrand, Complex Daubechies Wavelets, App. Comp. Harmonic Anal., vol.2, p.219, 1995.
- [15] J.M. Lina, Image processing with Complex Daubechies Wavelets, Int. J. of Mathematical Imaging and Vision, vol.7, p.211, 1997.
- [16] J.M. Lina, Complex Daubechies Wavelets: filters design and applications, First ISSAC Conf., Delaware, 1996.
- [17] J.M. Lina and P. Drouilly, The importance of the phase of the symmetric Daubechies Wavelets representation of signals, Proc. IWISP'96, Manchester (UK), p.69, 1996.
- [18] P.G. Lemarié, Une nouvelle base d'ondelettes de $L^2(\mathbb{R}^n)$, J. de Math. Pures et Appl., 67, p.227, 1988.
- [19] S. Mallat, *A Wavelet Tour of Signal Processing*, Acad. Press Pub., 1998.
- [20] K.S. Miller, *Complex Stochastic Processes*, Addison-Wesley Pub., 1974.
- [21] B. Picinbono, Second-Order Complex Random Vectors and Normal Distributions IEEE Trans. Sig. Proc. **44**, p.2637, 1996.
- [22] J. Stromberg, A modified Franklin system and higher order spline systems on \mathbb{R}^n as unconditional bases for Hardy spaces, Conference in honor of A. Zygmund, Vol.II, Wadsworth math. series, p.475, 1982.

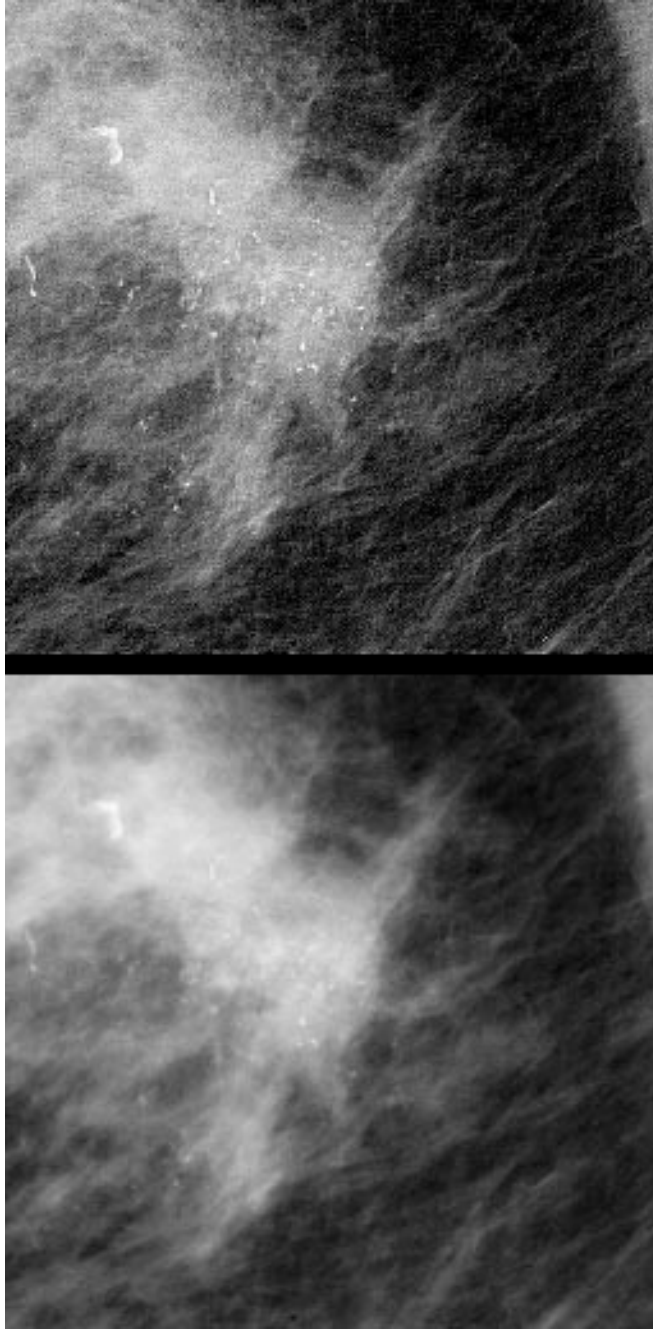


Figure 24: Image Enhancement: The test image (bottom) is a region of a digitized mammography. The upper image has been synthesized using S with $SDW4$ and $N=3$.